Supplementary Information

Data-Driven Structural Angle Mining Elucidates Hidden Design Rules for Hydrogen Evolution Single-Atom Electrocatalysts

Bingqing Ge[+acd], Yang Chen[+b] , Yidi Wu[+ac], Fenfei Wei[cd], Fengyu Li[f], Lulu Chen[ac], Jian Lin[*b] , Xianzhi Fu[ac] and Sen Lin[*ace]

[a]State Key Laboratory of Chemistry for NBC Hazards Protection, College of Chemistry, Fuzhou University, Fuzhou 350116, China

[b]CAS Key Laboratory of Science and Technology on Applied Catalysis, Dalian Institute of Chemical Physics, Chinese Academy of Sciences, Dalian 116023, China

[c]State Key Laboratory of Photocatalysis on Energy and Environment, College of Chemistry, Fuzhou University, Fuzhou 350002 China

[d]Key Laboratory of Mesoscopic Chemistry, School of Chemistry, Nanjing University, Nanjing 210023, Jiangsu, China

[e]College of Chemistry and Chemical Engineering, Institute for Green Chemistry and Environmental Science, Inner Mongolia University, Hohhot 010021, China

[f]Research Center for Quantum Physics and Technologies, School of Physical Science and Technology, Inner Mongolia University, Hohhot, 010021, China

[+] These authors contributed equally to this work.

*Email: jianlin@dicp.ac.cn, slin@fzu.edu.cn

Table of Contents

Computational methods

All spin-polarized DFT calculations were performed using the Vienna *ab initio* simulation package (VASP) based on plane-wave basis sets.[1] The VASPKIT[2] was used as the post-processing package to process and analyze the data output by VASP. The combination of the projected augmented wave (PAW) method[3] and the generalized gradient approximation (GGA)[4] with the PBE functional is employed to describe the exchange-correlation interactions among electrons, ions, and electron self-interactions.[5] The plane-wave expansion cut off energy is set to 400 eV, and the convergence criteria for energy and force in electronic iteration steps are 10^{-4} eV and 0.02 eV/Å, respectively. A 5 × 5 × 1 supercell was chosen after convergence testing with a vacuum layer set in the z direction with a minimum thickness of 20 Å to avoid interactions between periodic layers. Van der Waals weak interactions were also considered in the calculations, described using the DFT-D3 dispersion correction.[6] When sampling the first Brillouin zone of the reciprocal space (K-space), we utilized a 2 × 2 × 1 grid based on the Monkhorst−Pack scheme.[7] The adsorption energy (E_{ads}) and the corresponding Gibbs free energy (ΔG) for the binding of different reaction intermediates to the surface are calculated using the following formulas:[8–10]

$$E_{ads} = E_{*A} - E_{*} - E_{A} \quad (1)$$

$$\Delta G = \Delta E + \Delta E_{ZPE} - T\Delta S \quad (2)$$

In the formula for calculating E_{ads}, E_A represents the energy of the adsorbate, while E_* and E_{*A} represent the total energies before and after adsorption on the transition metal dichalcogenides (TMDs) surface, respectively. For the calculation of the free energy, ΔE is the energy difference obtained from DFT calculations between the products and reactants. ΔE_{ZPE} and ΔS represent the change in zero-point energy and entropy, respectively.

Catalytic activity is usually measured by the key indicator of overpotential (η). A smaller overpotential indicates superior catalytic performance.[11] For HER, the overpotential is determined by the absolute value of the hydrogen adsorption Gibbs free

92 energy (ΔG_{*H}),[12] where an ideal catalyst exhibits $\Delta G_{*H} \approx 0$ eV.[13,14] For OER, the
93 overpotential arises from the potential-determining step, which is calculated using the
94 following expression:

$$\Delta G_1 = G_{*OH} + 1/2G_{H_2} - G_{H_2O} - G_* \quad (3)$$

$$\Delta G_2 = G_{*O} + 1/2G_{H_2} - G_{*OH} \quad (4)$$

$$\Delta G_3 = G_{*OOH} + 1/2G_{H_2} - G_{*O} - G_{H_2O} \quad (5)$$

$$\Delta G_4 = 4.92 - \Delta G_1 - \Delta G_2 - \Delta G_3 \quad (6)$$

95 $\eta_{OER} = \max[\Delta G_1, \Delta G_2, \Delta G_3, \Delta G_4]/e - 1.23$ V.[8]

96 SISSO was adopted to conduct the training of the catalytic activity model. The
97 Pearson correlation coefficient was utilized to evaluate the independence of features,
98 and the formula is as follows.[15]

$$r = \frac{\sum_i (x_i - \bar{x})(y_i - \bar{y})}{\sqrt{\sum_i (x_i - \bar{x})^2 \sum_i (y_i - \bar{y})^2}} \quad (7)$$

99 Here, x and y are the compared features. The coefficient r lies between –1 and 1.
100 Values approaching –1 correspond to strong negative linear correlation; values
101 approaching 1 correspond to strong positive linear correlation; and values approaching
102 0 indicate negligible linear correlation.

103 Catalyst preparation

104 Materials: the source and purity of the chemicals used are as follows: H_2IrCl_6
105 (Aladdin, Ir≧36%), vanadlum chlorlde (Aladdin, >96%). thiourea (Aladdin, >99%),
106 isopropanol (Aladdin, AR 99.7%), and MoS_2 (XFNANO, thickness 1-5nm).

107 Synthesis of $Ir_1@MoS_2$: Firstly, 0.15 mL H_2IrCl_6 solution was added into 1.0 mL
108 of 0.5mM thiourea solution. The resulting solution was then introduced into 30 mL of
109 a water/isopropanol mixture (1:3, v/v) containing 30 mg of MoS_2. The suspension was
110 sonicated for 6 h and subsequently stirred for another 6 h. Finally, the precipitate was

collected, thoroughly rinsed with deionized water, and dried under vacuum to obtain the $Ir_1@MoS_2$ product.

$V_1@MoS_2$ was synthesized via a one-step hydrothermal method. Firstly, 1.0 mmol of $(NH_4)_6Mo_7O_{24}\cdot 4H_2O$ and 30 mmol of thiourea ($CS(NH_2)_2$) were dissolved in 35 mL of deionized water under stirring. Then, 2 mL of a 1.0 mg mL^{-1} VCl_3 solution was added dropwise to the above solution and the mixture was stirred for 10 min. The resulting solution was transferred into a Teflon-lined stainless-steel autoclave and heated at 180 °C for 24 h. The black precipitate was collected and washed several times with deionized water and ethanol, and then dried at 60 °C to obtain the $V_1@MoS_2$ product.

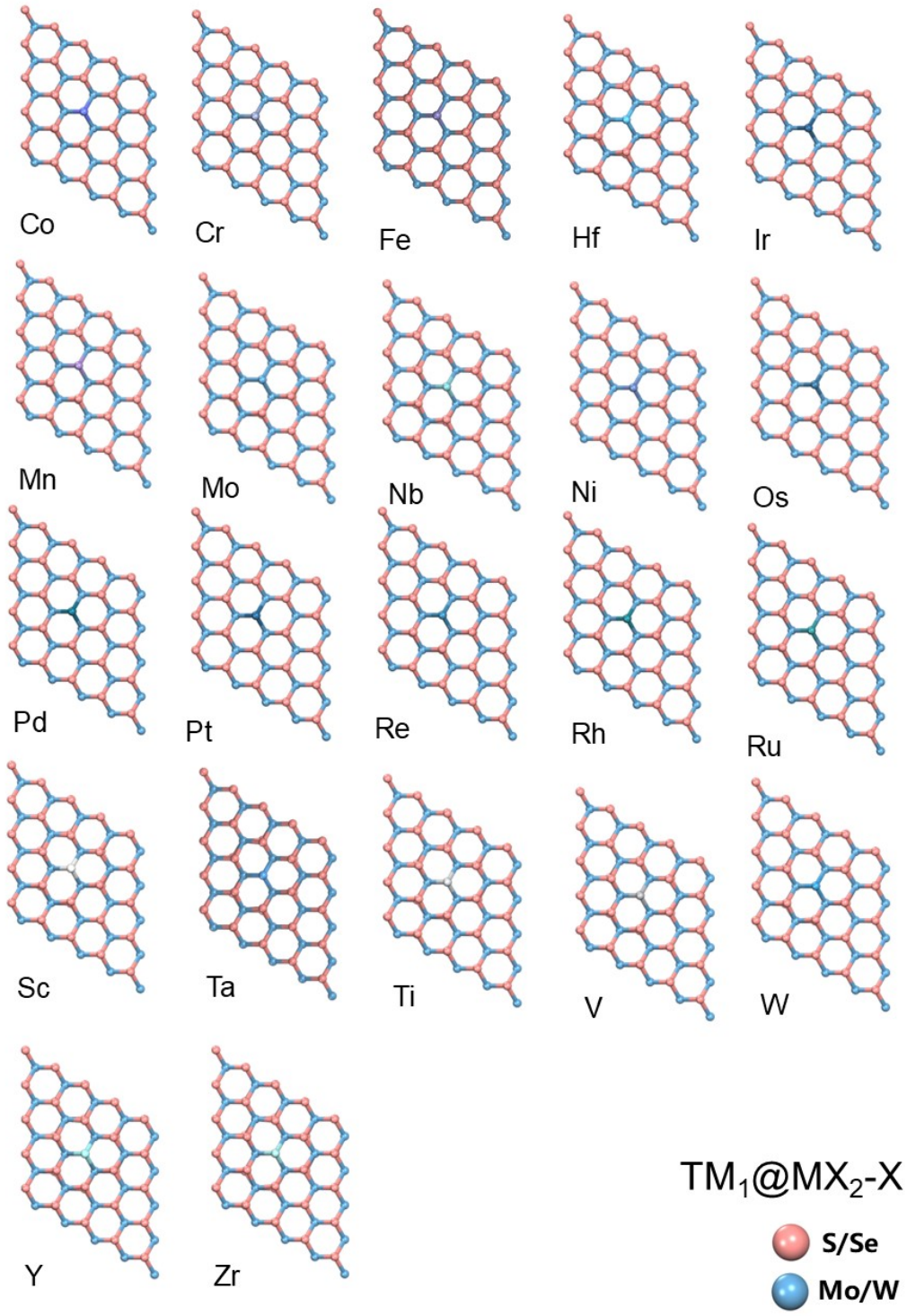

122

123 **Figure S1.** All the structure of $TM_1@MX_2$-X (chalcogen-vacancy).

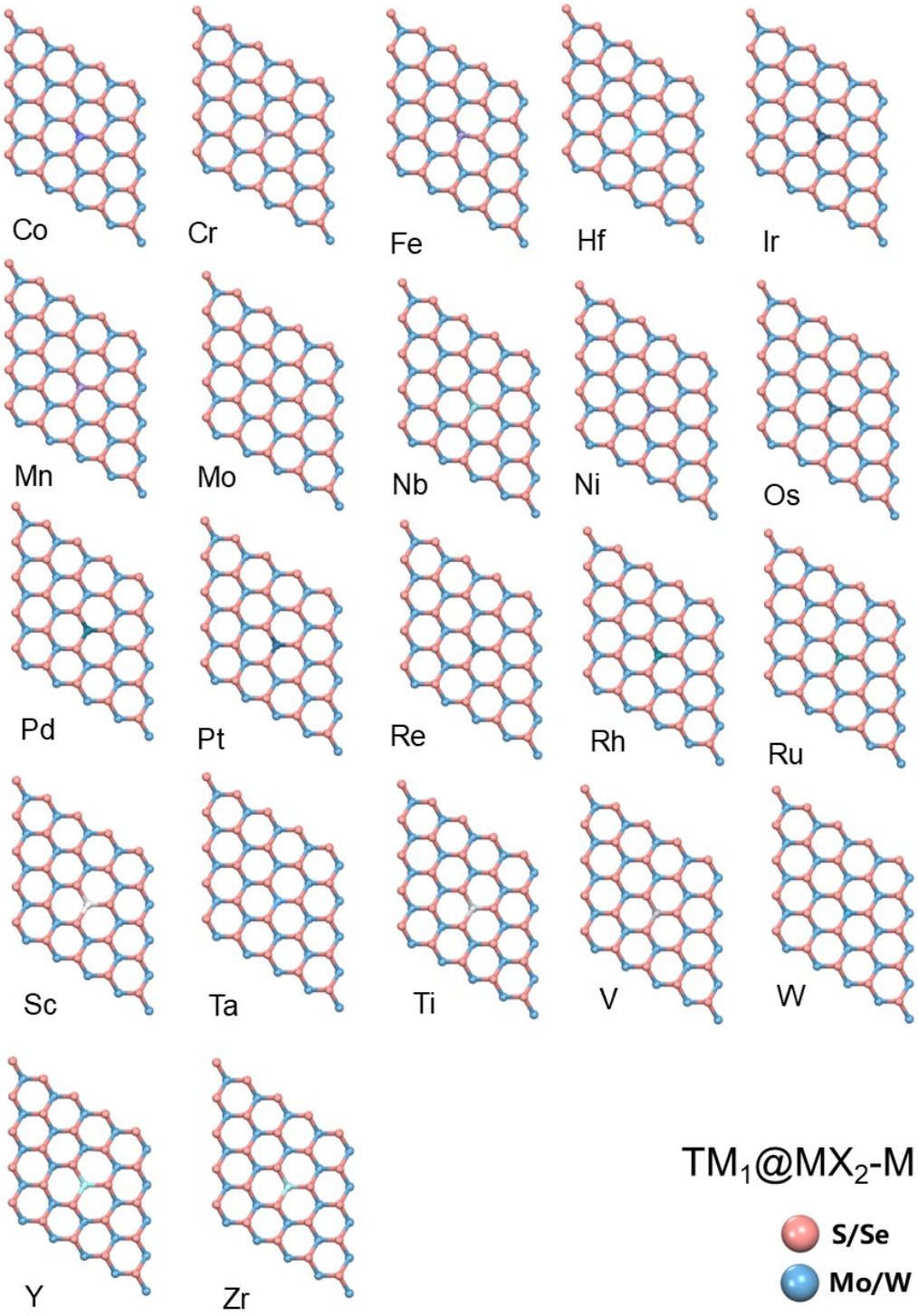

Figure S2. All the $TM_1@MX_2$-M structures (metal-vacancy).

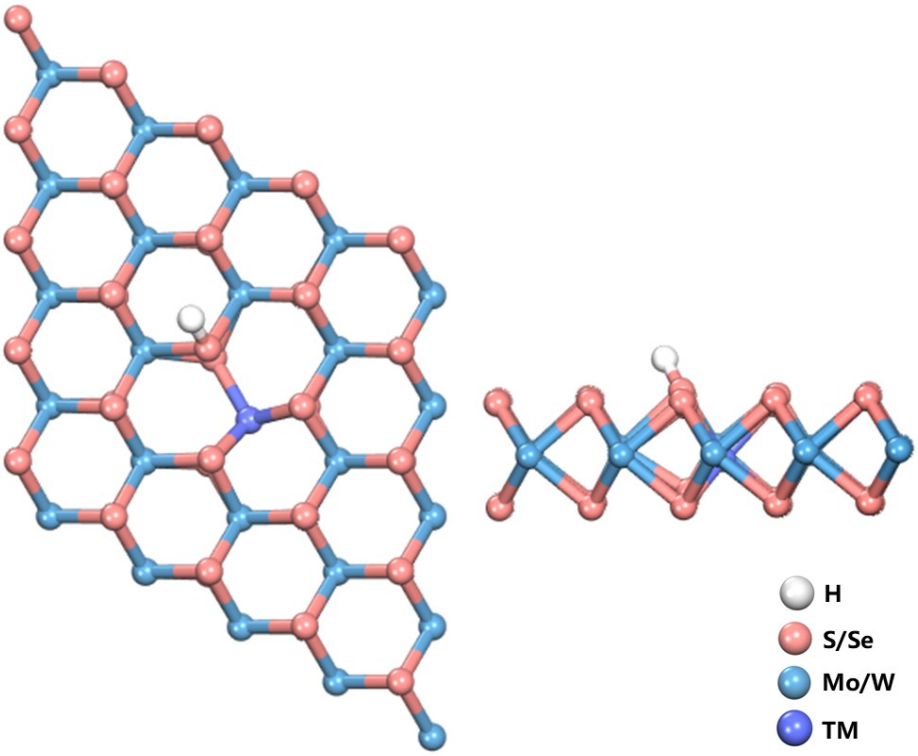

Figure S3. The H adsorption site on $TM_1@MX_2$-M (metal-vacancy).

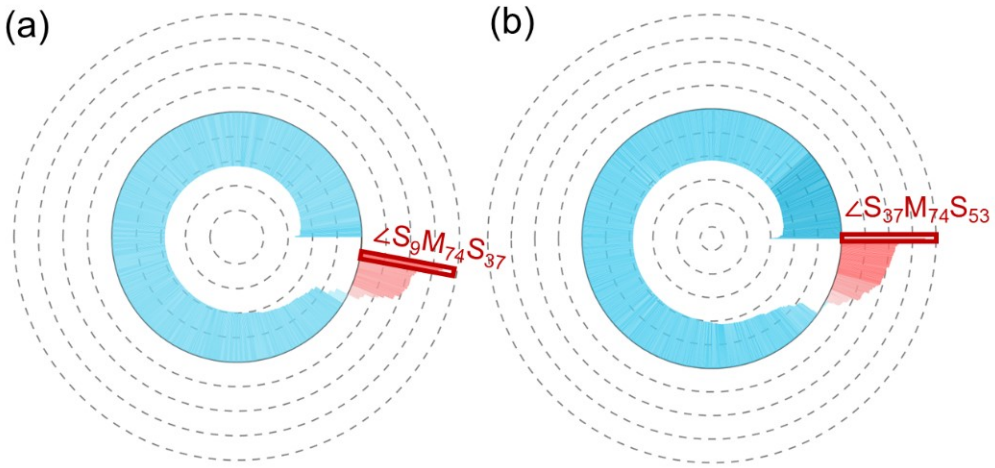

Figure S4. Correlation analysis of structural distortions with HER activity for TM_1@MoS_2. Pearson correlation coefficients (r) between ΔG_{*H} and doped metal-centered angles (vertex at M_{74}) for (a) vertical, and (b) internal distortion modes (dark red: strong positive, $r \approx +1$; dark blue: strong negative, $r \approx -1$).

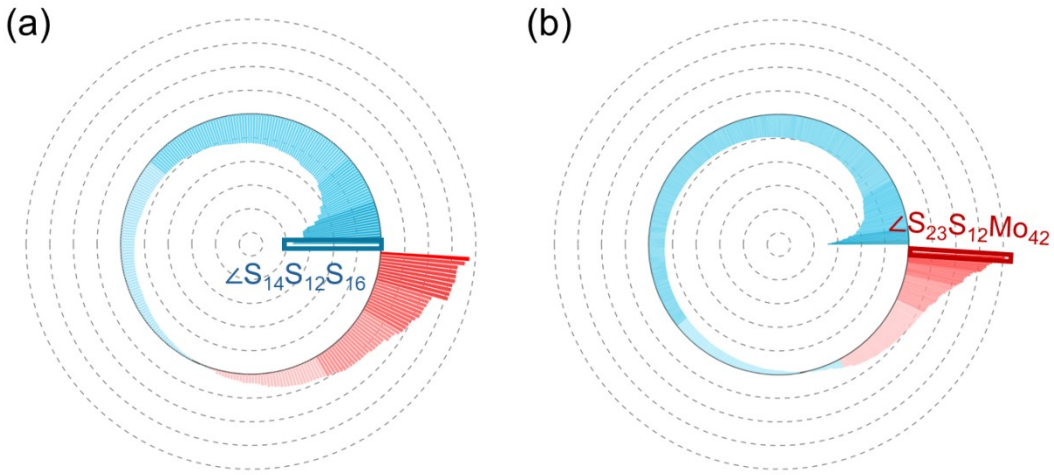

Figure S5. Correlation analysis of structural distortions with HER activity for $TM_1@MoS_2$. Pearson correlation coefficients (r) between ΔG_{*H} and first-shell sulfur-centered angles (vertex at S_{12}) for (a) surface, (b) vertical distortion modes.

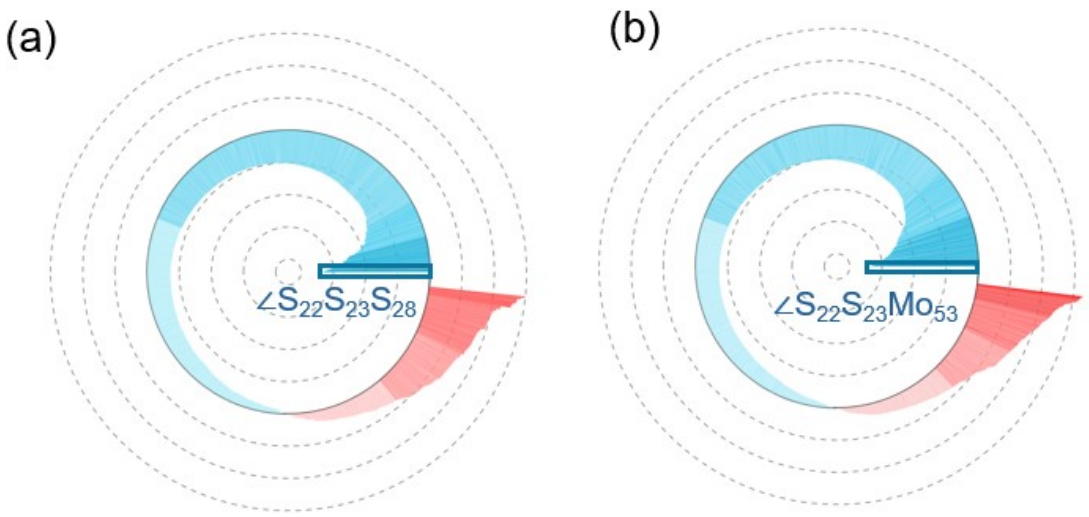

Figure S6. Correlation analysis of structural distortions with HER activity for TM_1@MoS_2. Schematic diagram of Pearson correlation coefficient (r) between ΔG_{*H} and the second-shell S (vertex at S_{23}) atoms-centered angles for (a) vertical, and (b) internal distortion modes.

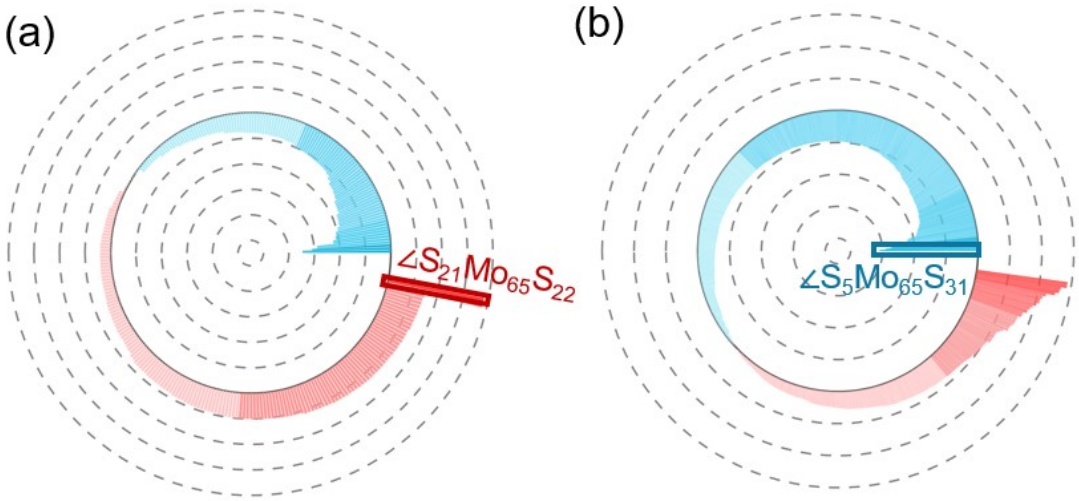

Figure S7. Correlation analysis of structural distortions with HER activity in TM_1@MoS_2. Schematic diagram of Pearson correlation coefficient (r) between ΔG_{*H} and the Mo (vertex at Mo_{65}) atoms-centered angles for (a) surface, and (b) vertical distortion modes.

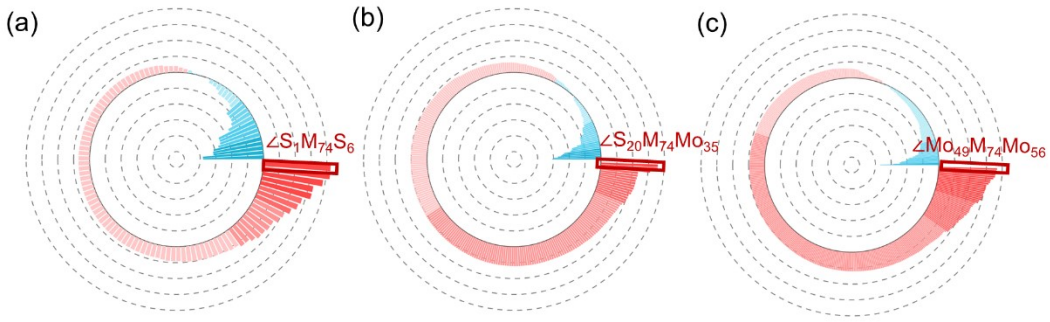

Figure S8. Correlation analysis of structural distortions with OER activity in TM_1@MoS_2. Pearson correlation coefficients (*r*) between overpotential and doped metal-centered angles (vertex at M_{74}) for (a) surface, (b) vertical, and (c) internal distortion modes.

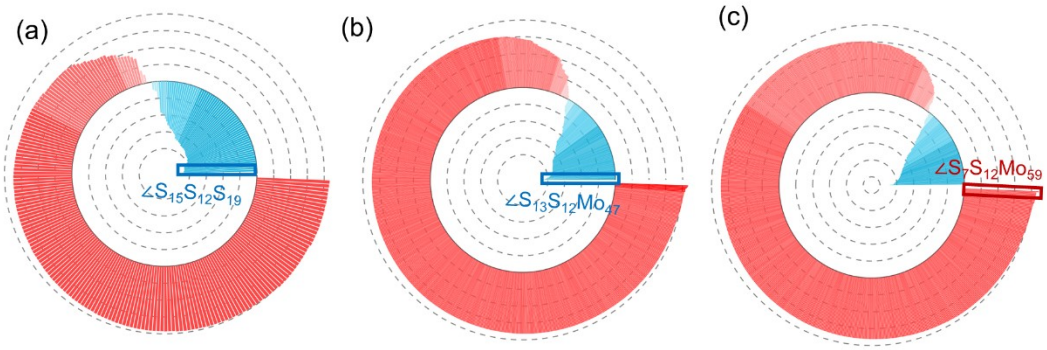

158

159 **Figure S9.** Correlation analysis of structural distortions with OER activity in TM_1@
160 MoS_2. Pearson correlation coefficients (*r*) between overpotential and first-shell sulfur-
161 centered angles (vertex at S_{12}) for (a) surface, (b) vertical, and (c) internal distortion
162 modes.

163

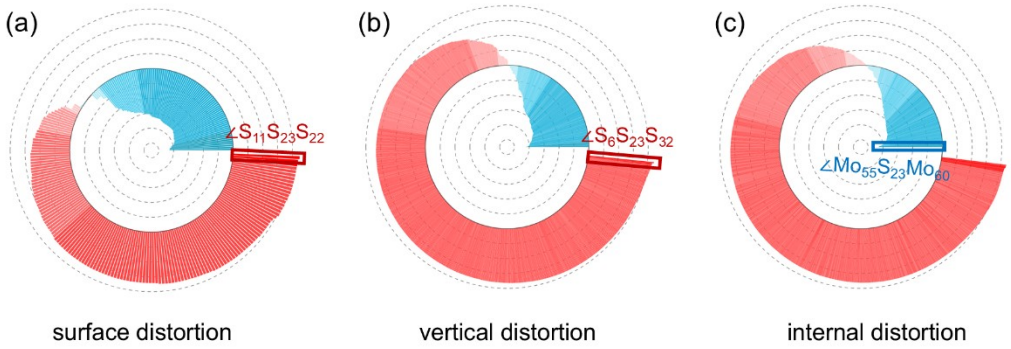

Figure S10. Correlation analysis of structural distortions with OER activity in TM_1@MoS_2. Pearson correlation coefficients (r) between overpotential and second-shell sulfur-centered angles (vertex at S_{23}) for (a) surface, (b) vertical, and (c) internal distortion modes.

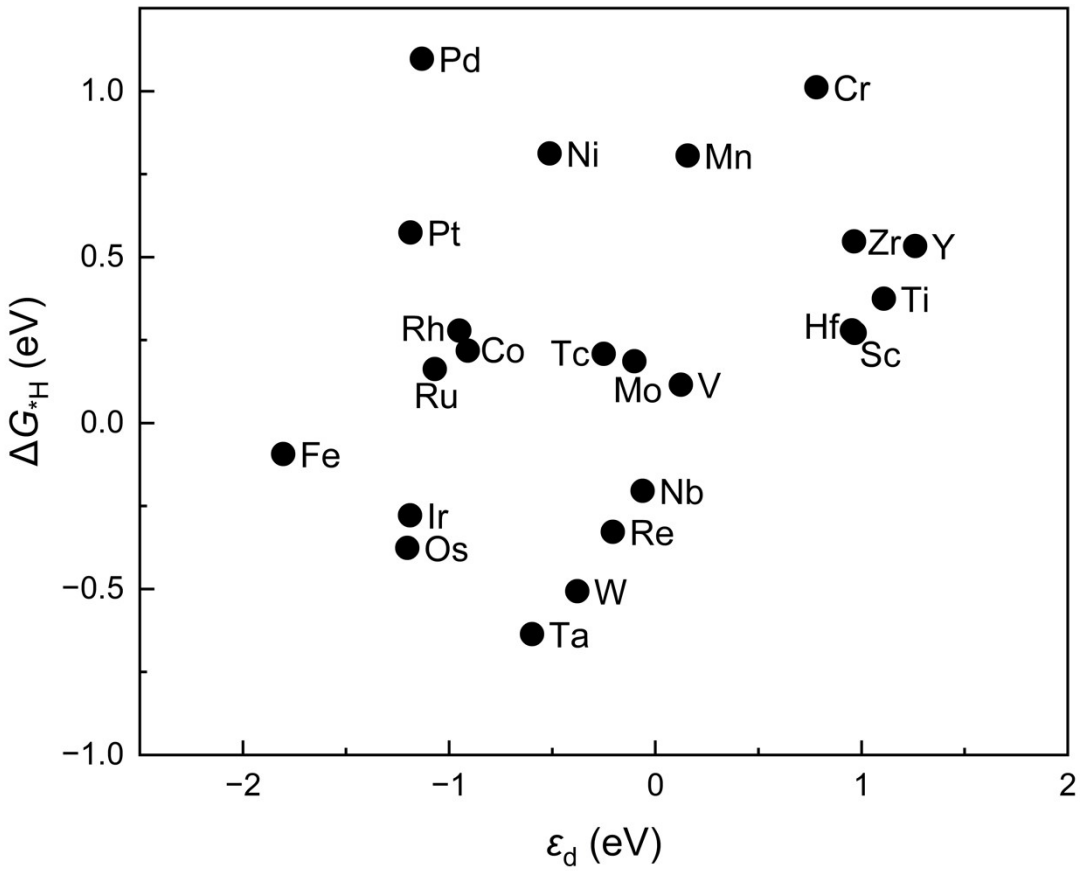

170

171 **Figure S11.** The relationship between *d*-band center (ε_d) of TM_1 and ΔG_{*H} for TM_1@

172 MoS_2-S.

173

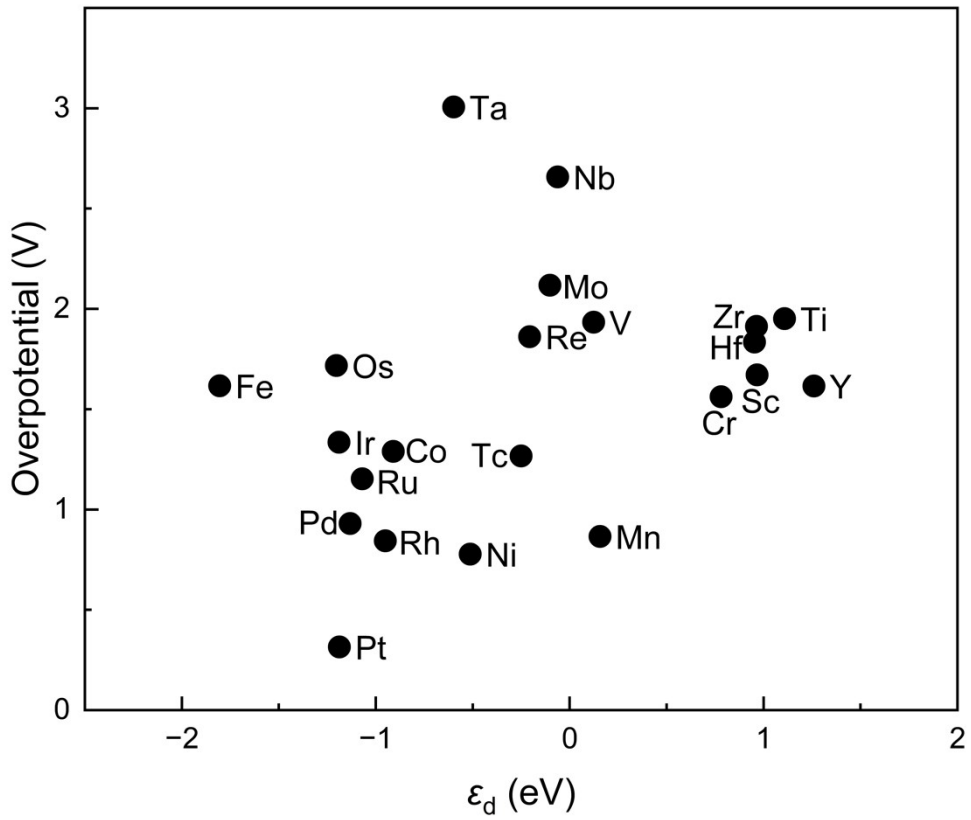

Figure S12. The relationship between ε_d of TM_1 and OER overpotential for TM_1@ MoS_2-S.

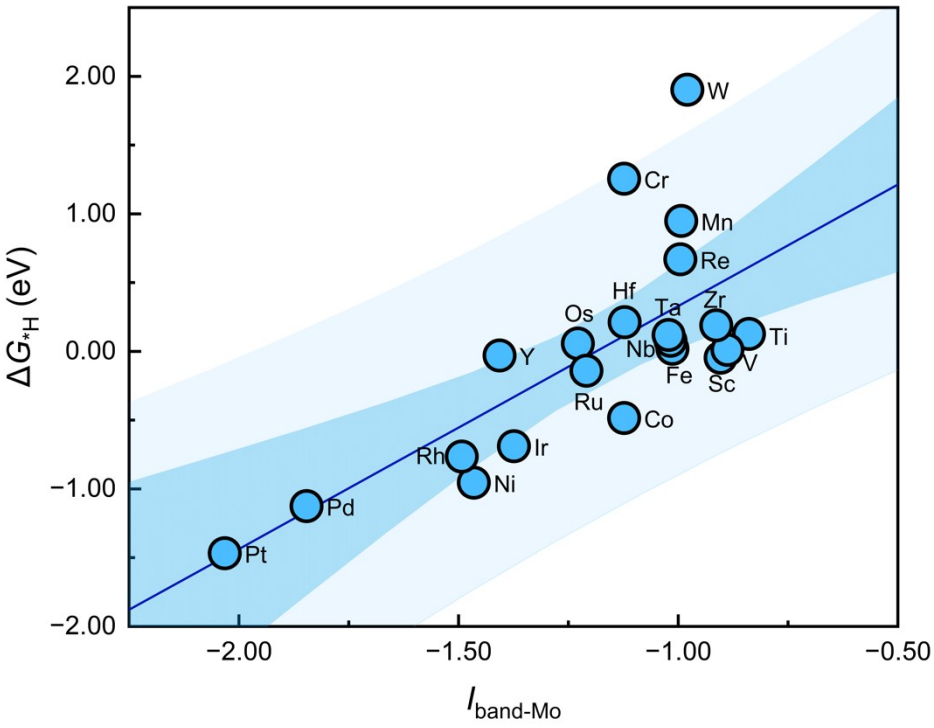

Figure S13. The linear relationship between $I_{band\text{-}Mo}$ and ΔG_{*H} for $TM_1@MoS_2$-Mo.

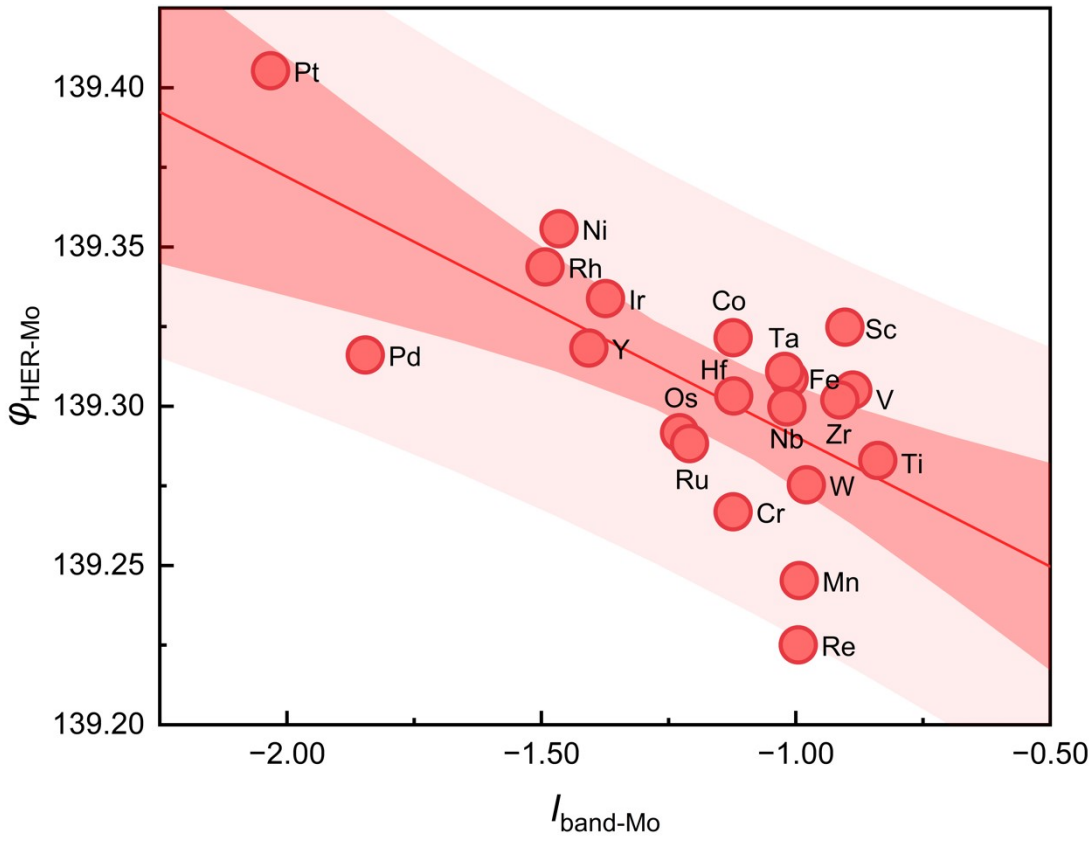

182

183 **Figure S14.** The linear relationship between $I_{band\text{-}Mo}$ and $\varphi_{HER\text{-}Mo}$ for $TM_1@MoS_2$-Mo.

184

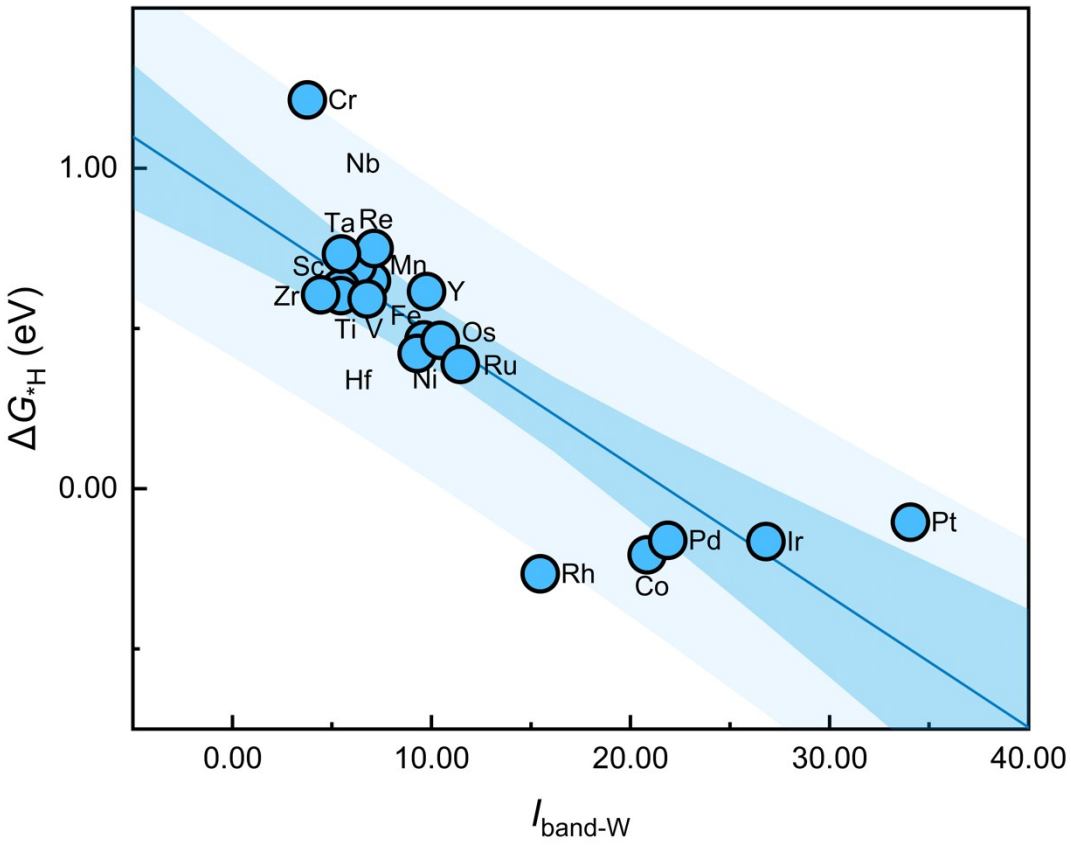

185

186 **Figure S15.** The linear relationship between $I_{band\text{-}W}$ and ΔG_{*H} for $TM_1@WSe_2$-W.

187

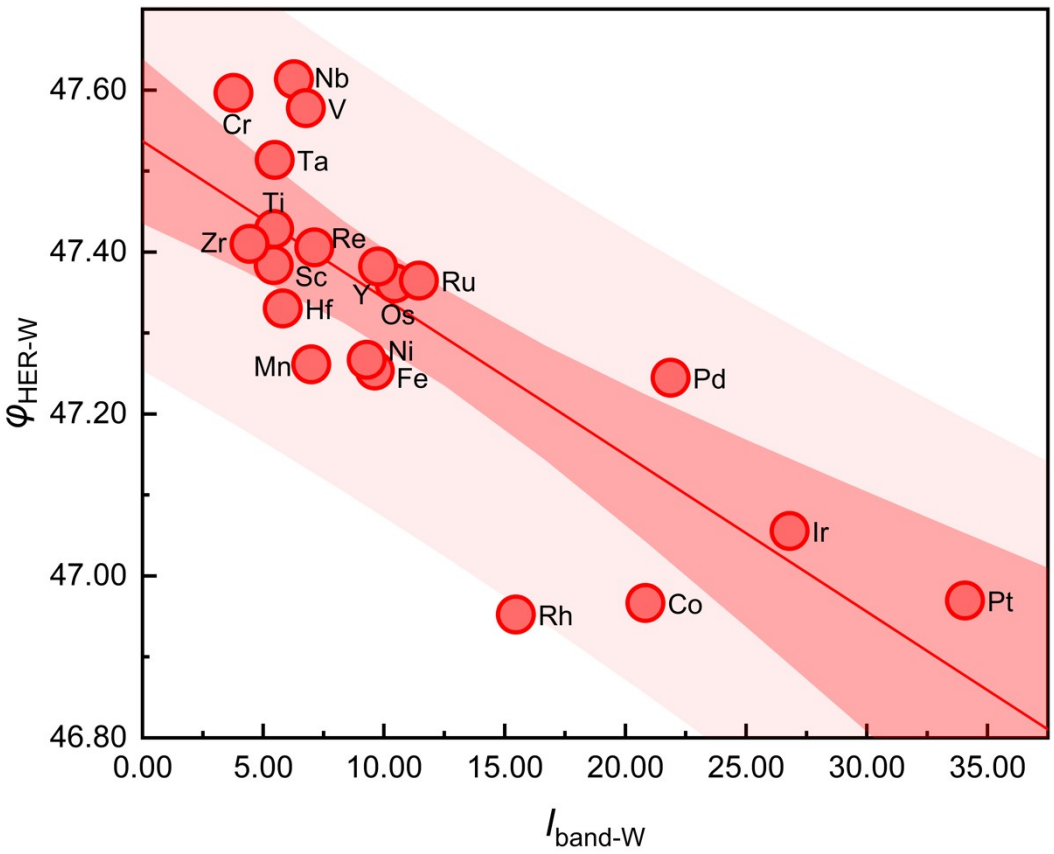

188

189 **Figure S16.** The linear relationship between I_{band-W} and φ_{HER-W} for $TM_1@WSe_2$-W.

190

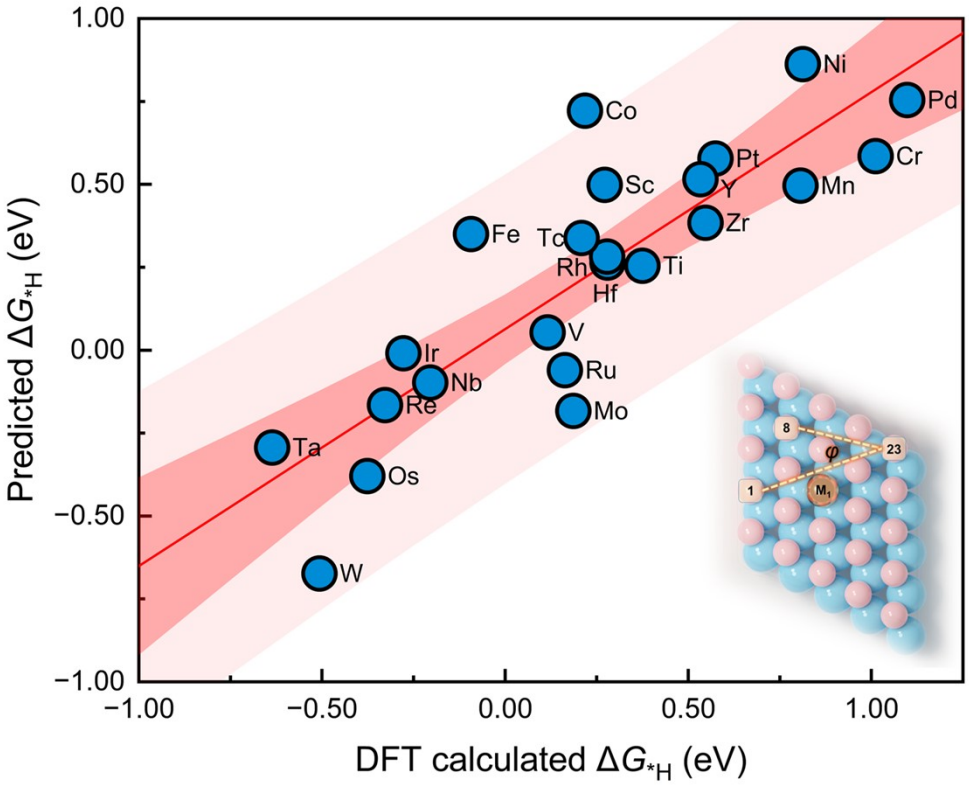

191

192 **Figure S17.** The relationship between predicted HER activities and DFT-computed
193 values in $TM_1@MoS_2$-S system ($\angle S_1S_{23}S_8$).

194

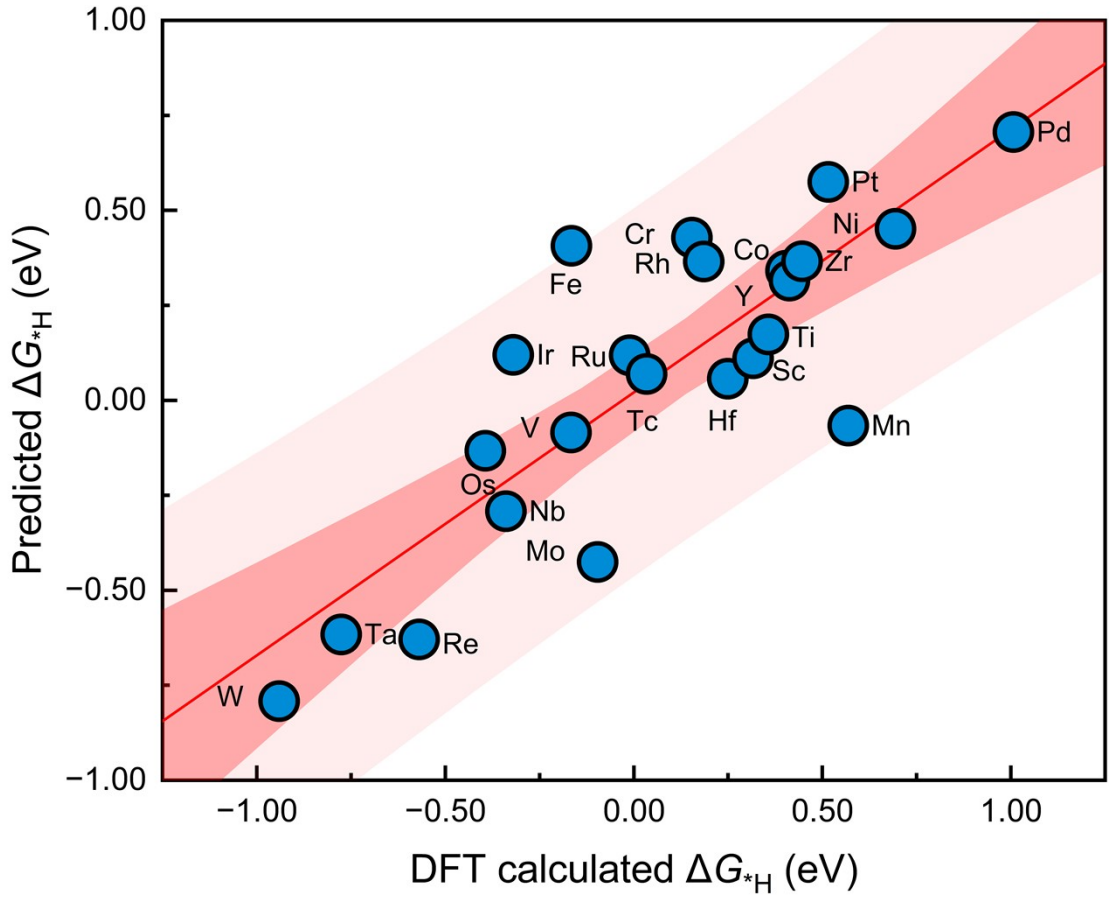

Figure S18. The relationship between predicted HER activities and DFT-computed values in $TM_1@WSe_2$-Se system ($\angle S_1S_{23}S_8$).

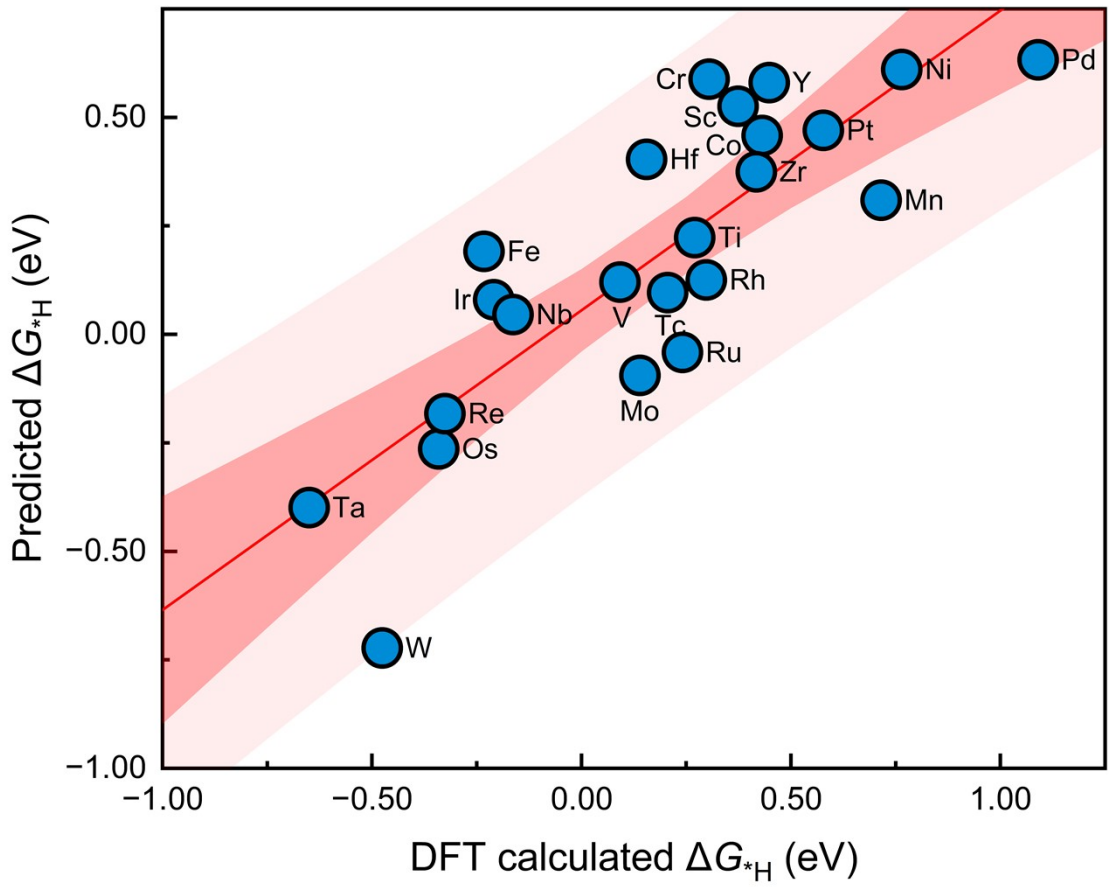

199

200 **Figure S19.** The relationship between predicted HER activities and DFT-computed
201 values in $TM_1@WS_2$-S system ($\angle S_1S_{23}S_8$).

202

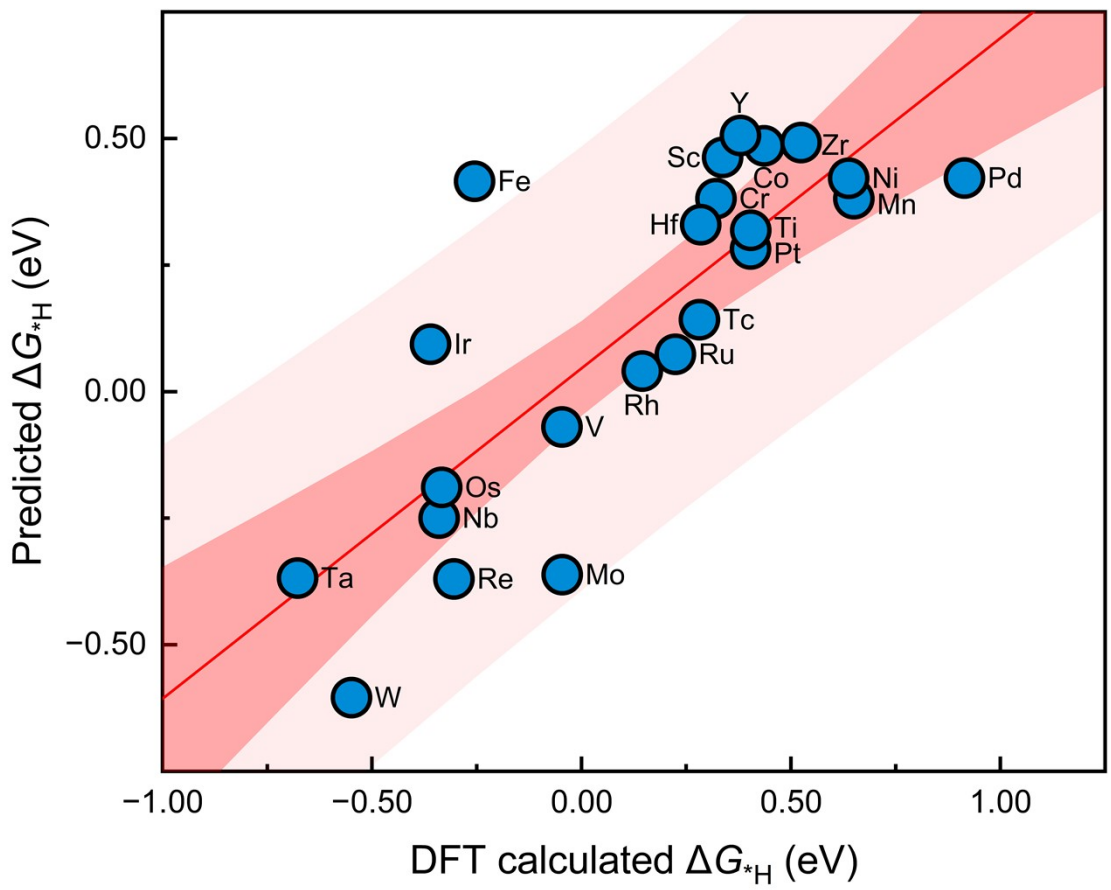

Figure S20. The relationship between predicted HER activities and DFT in TM_1@$MoSe_2$-Se system ($\angle S_1S_{23}S_8$).

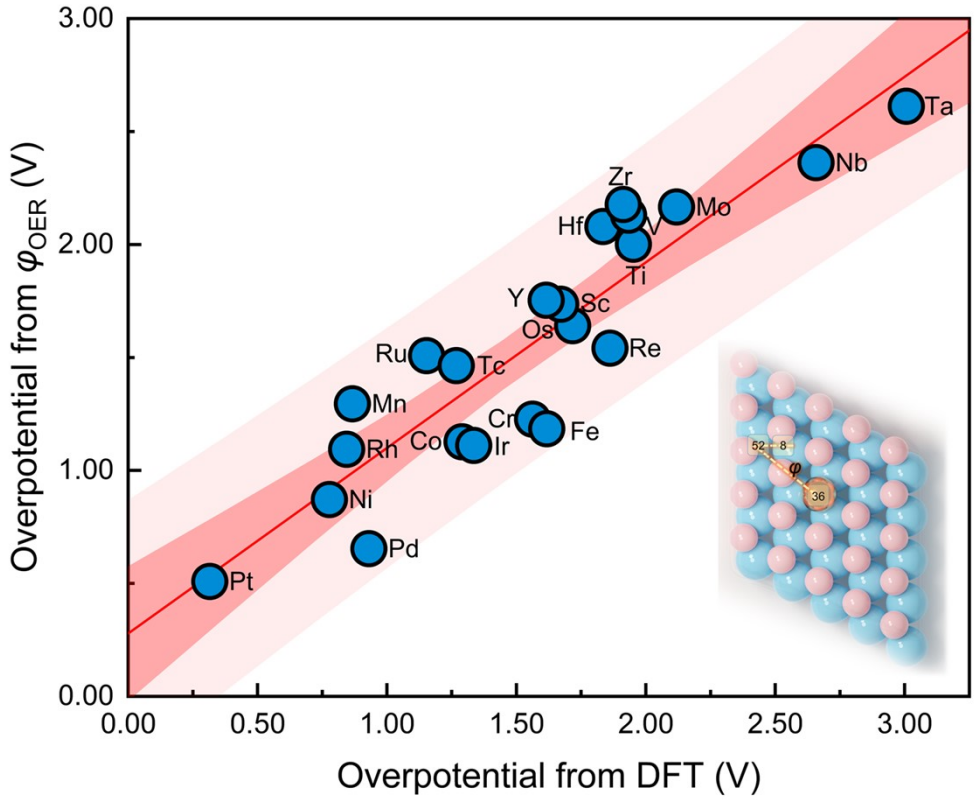

207

208 **Figure S21.** The relationship between predicted OER activities and DFT-computed
209 values in $TM_1@MoS_2$-S system ($\angle S_8Mo_{52}S_{36}$).

210

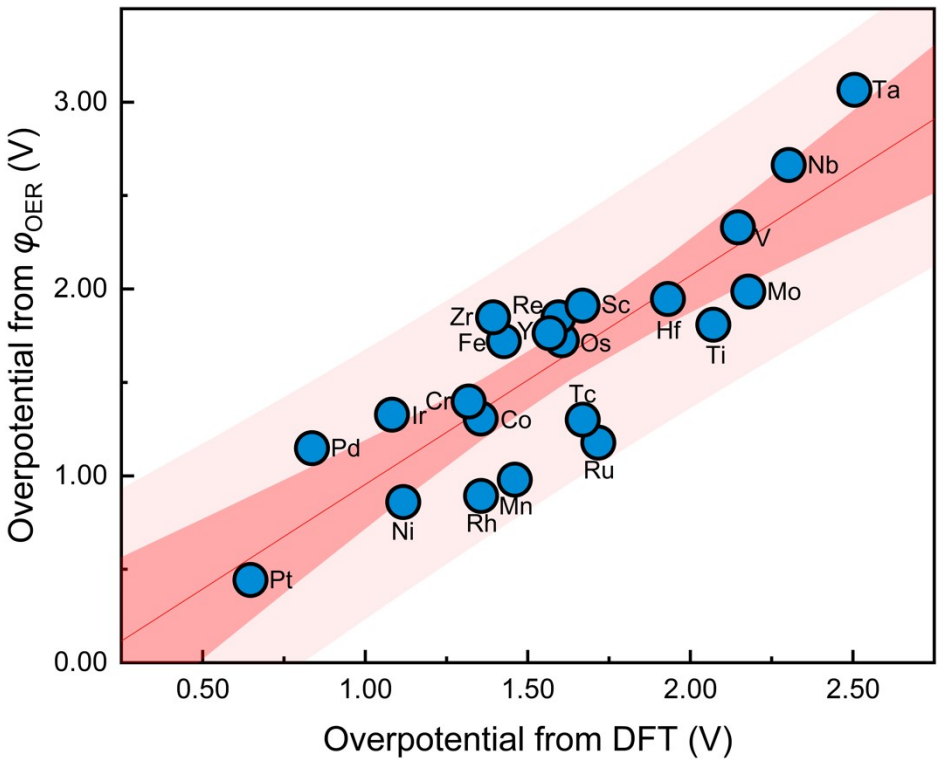

211

212 **Figure S22.** The relationship between predicted OER activities for φ_{OER} and
213 DFT-computed values in $TM_1@WS_2$-S system ($\angle S_8Mo_{52}S_{36}$).

214

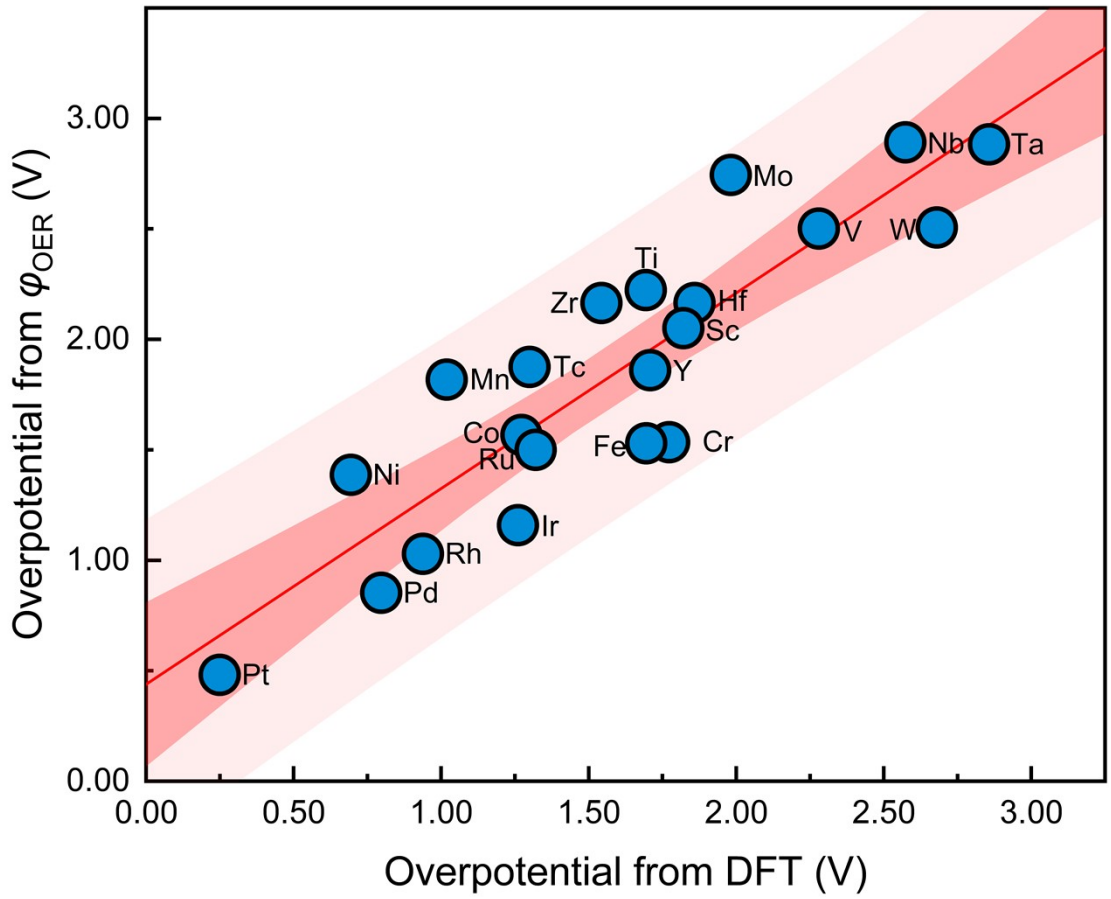

Figure S23. The relationship between predicted OER activities for φ_{OER} and DFT-computed values in $TM_1@WSe_2$-Se system ($\angle S_8Mo_{52}S_{36}$).

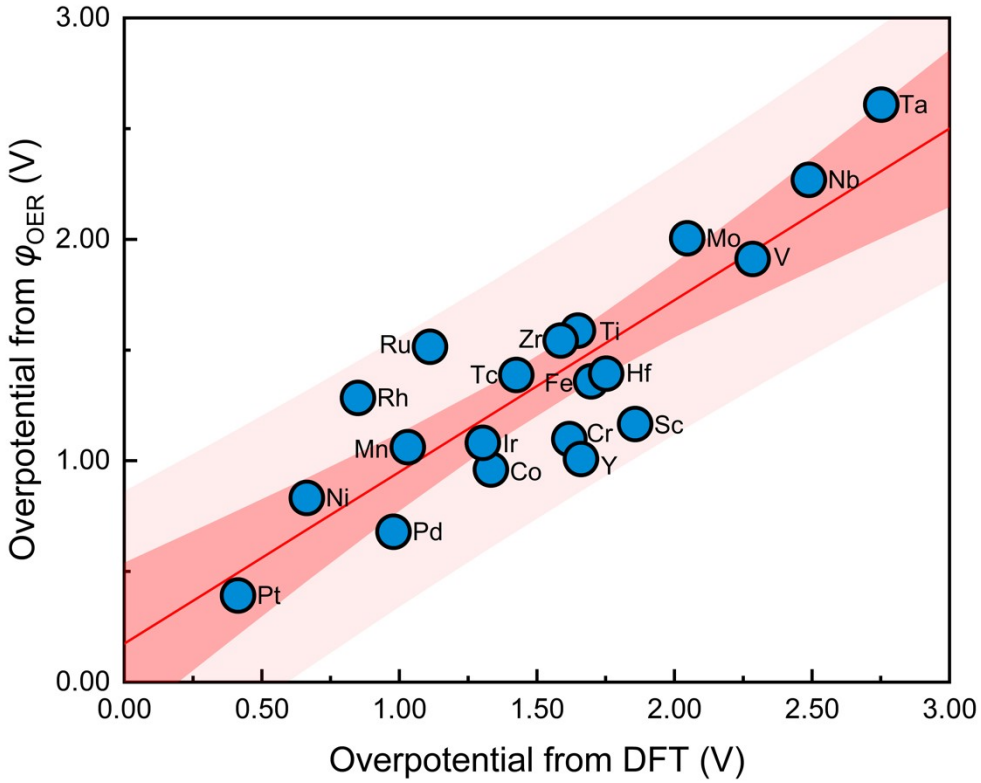

Figure S24. The relationship between predicted OER activities for φ_{OER} and DFT-computed values in TM_1@$MoSe_2$-Se system ($\angle S_8Mo_{52}S_{36}$).

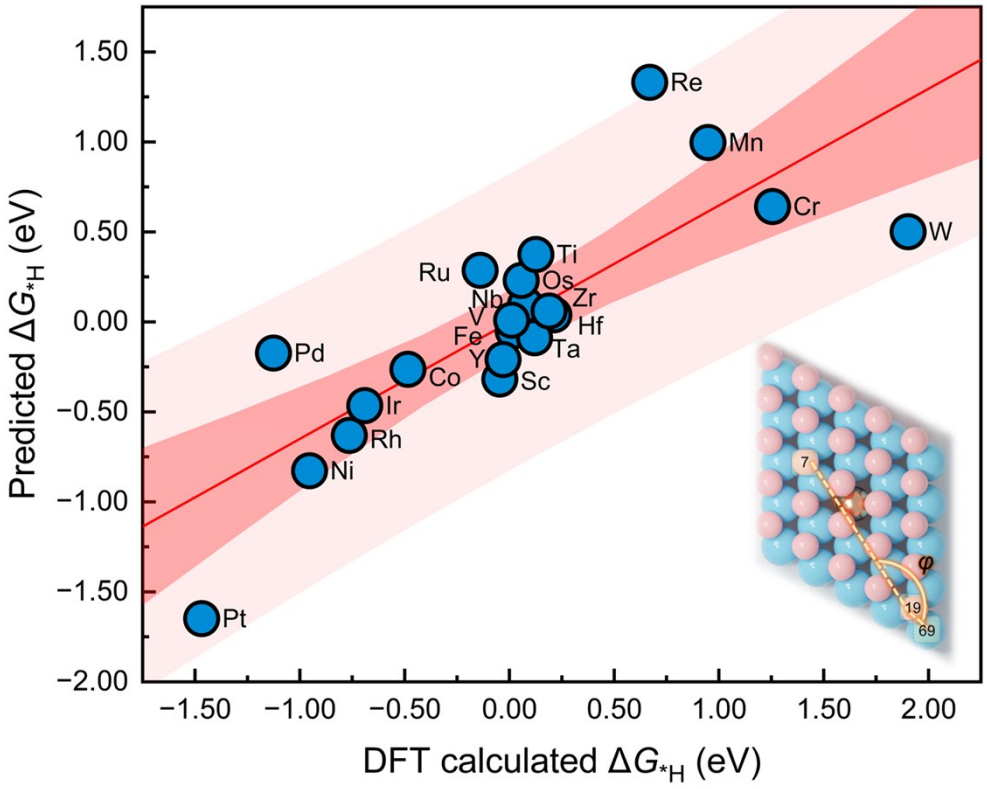

Figure S25. The relationship between predicted HER activities and DFT-computed values in $TM_1@MoS_2$-Mo system.

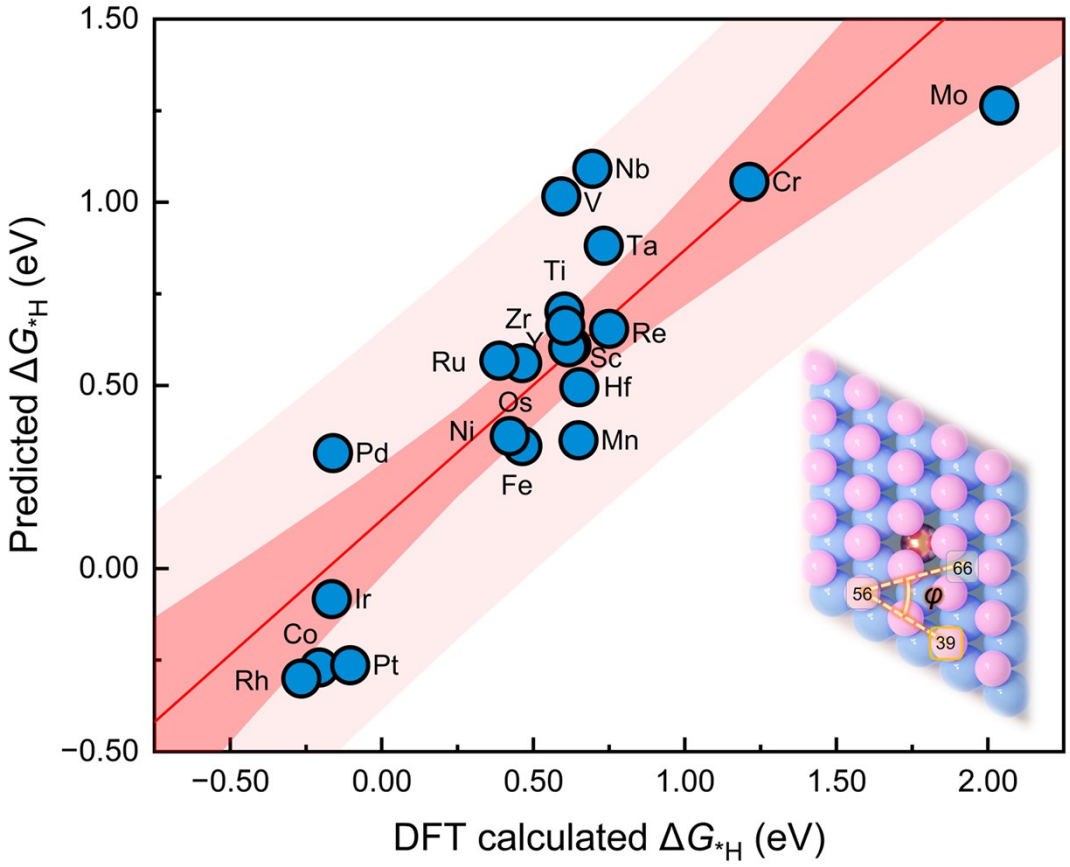

227

228 **Figure S26.** The relationship between predicted HER activities with DFT-computed
229 values in TM_1@WSe_2-W system.

230

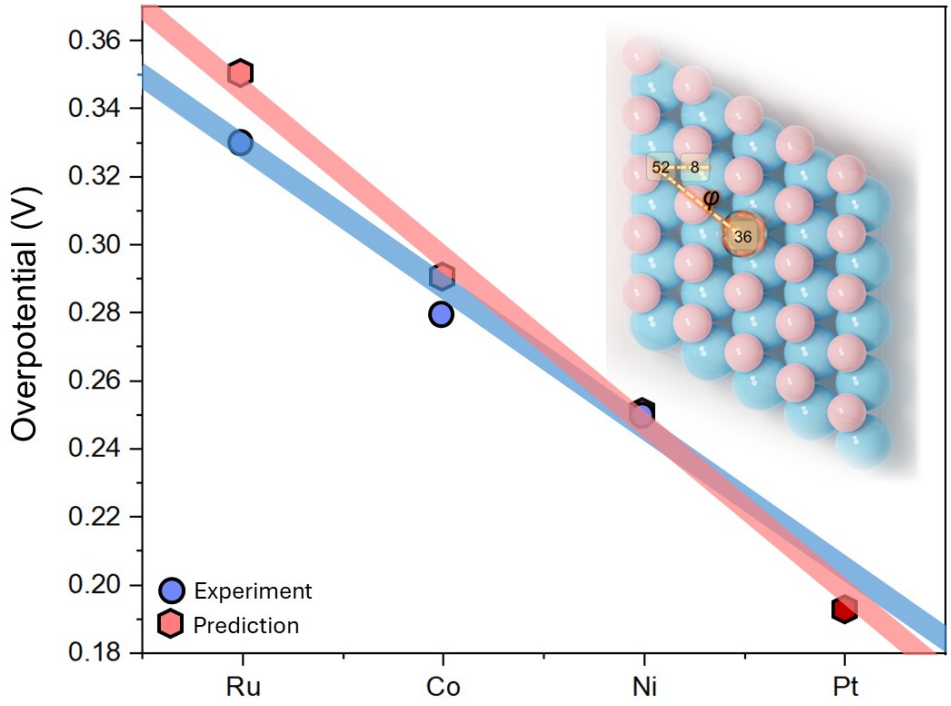

Figure S27. Comparison of experimental results and predicted OER overpotential results. The blue line shows the fit to the mean experimental activity, while the red line represents the fit to the predicted overpotentials.

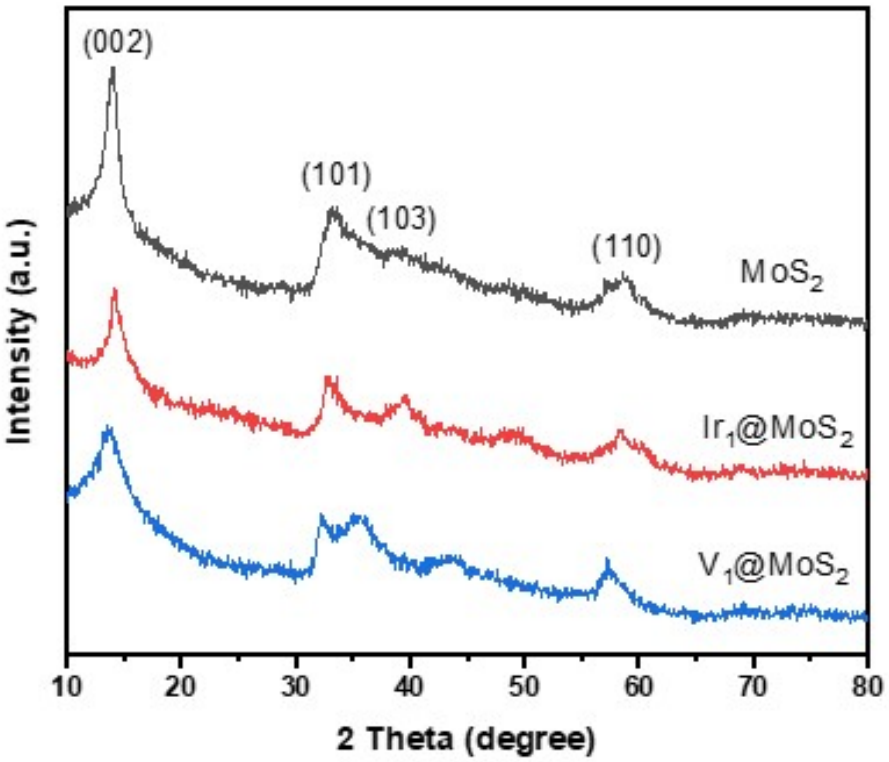

Figure S28. XRD patterns of the MoS_2, $Ir_1@MoS_2$ and $V_1@MoS_2$ catalysts.

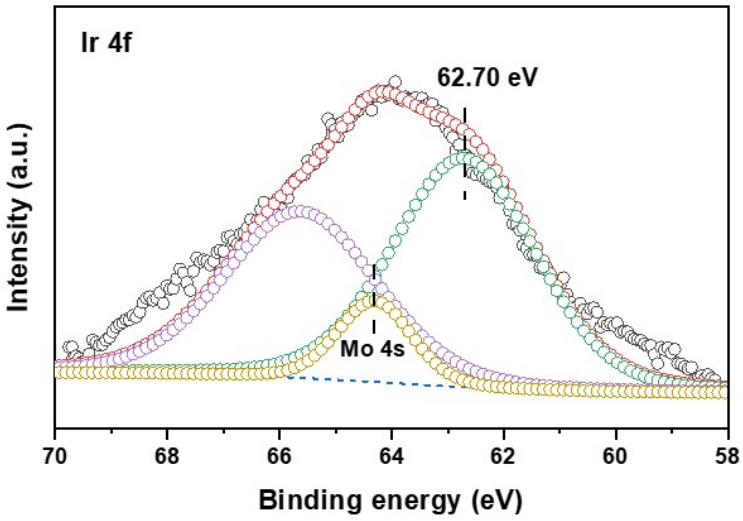

240

241 **Figure S29.** X-ray photoelectron spectra of Ir species.

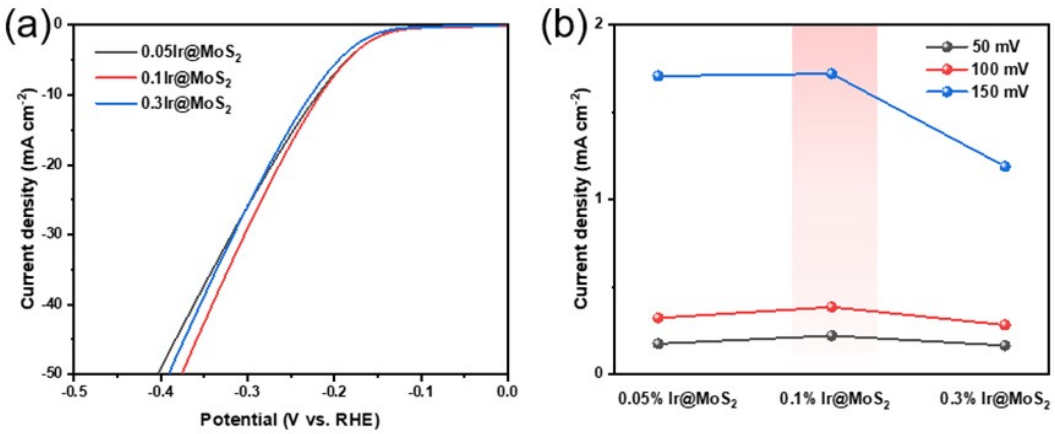

Figure S30. (a) HER polarization curves, and (b) Current densities at different overpotentials over the $Ir_1@MoS_2$ samples with different metal contents.

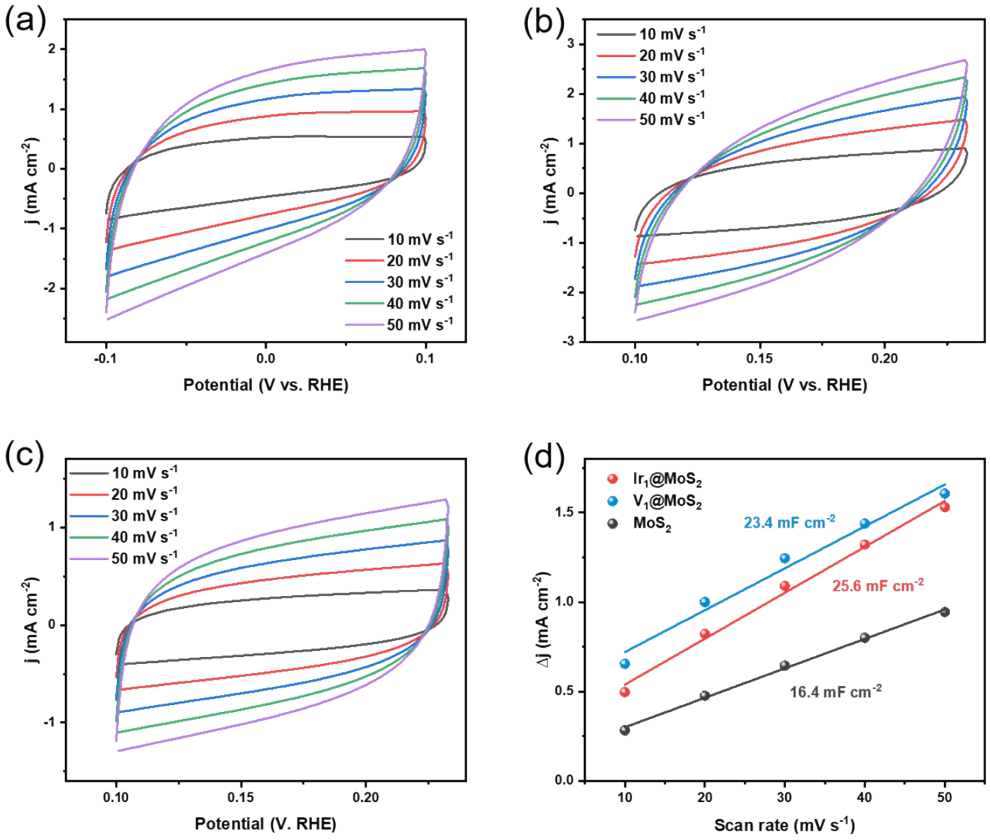

247

248 **Figure S31.** Current density plots against scan rates on (a) $Ir_1@MoS_2$, (b) $V_1@MoS_2$,
249 (c) MoS_2, and (d) current density differences plotted against scan rates.

250

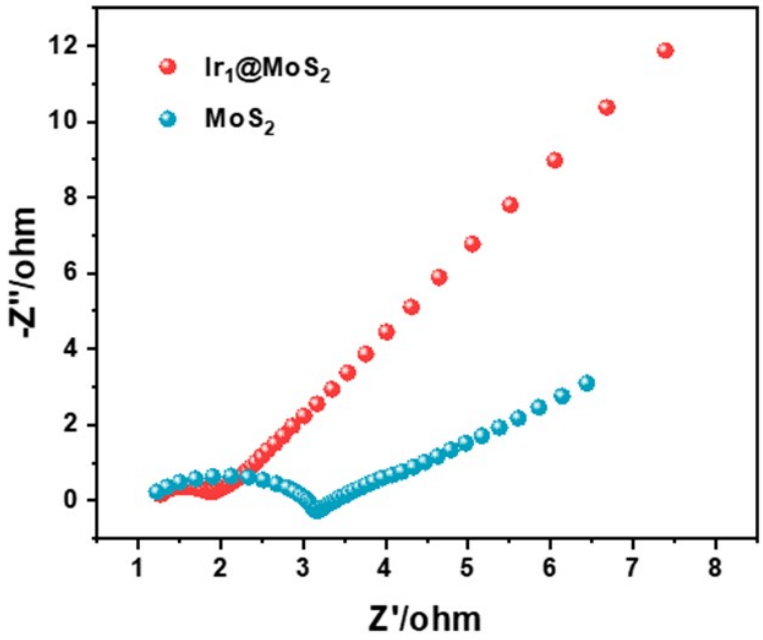

Figure S32. Electrochemical impedance spectroscopy evaluation for $Ir_1@MoS_2$ and MoS_2 samples.

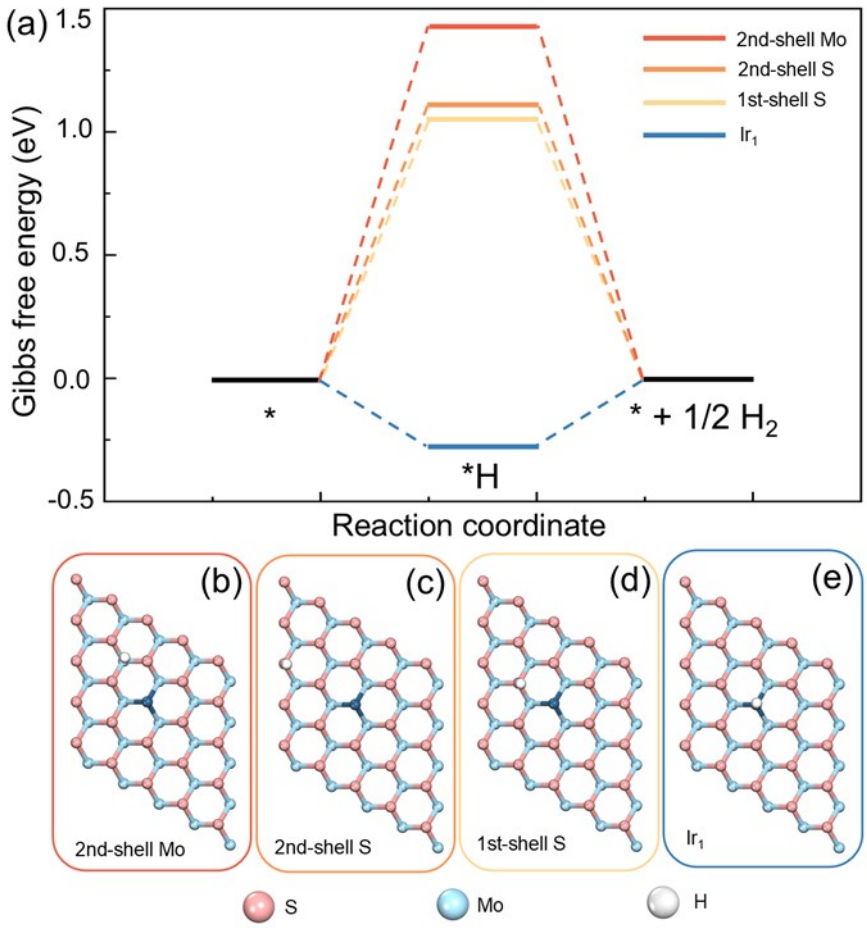

Figure S33. The reaction energy steps of the *H at different active sites in the Ir_1@MoS_2 catalyst for HER.

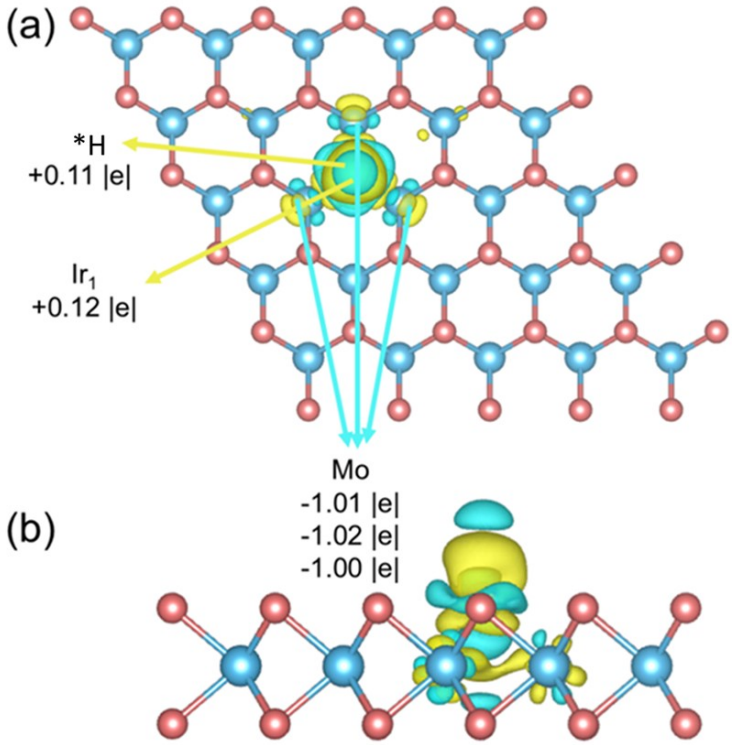

Figure S34. The differential charge density of Ir_1@MoS_2-S with H adsorbed. Yellow represents electron accumulation, and blue represents electron loss.

Table S1 Input features (band centers, eV) of SISSO of $TM_1@MoS_2$-S catalysts.

	M-s	M-d	S_{23}-p	S_1-s	S_{36}-p	Mo_{52}-s
Co	-1.272	-0.910	-2.531	-12.006	-2.513	-6.400
Cr	-0.464	0.781	-2.496	-11.998	-2.457	-6.394
Fe	-1.765	-1.805	-3.013	-12.516	-2.957	-6.903
Hf	-1.536	0.953	-2.224	-11.664	-2.100	-6.030
Ir	-1.654	-1.190	-2.337	-11.837	-2.281	-6.238
Mn	-0.475	0.157	-1.991	-11.519	-1.934	-5.902
Mo	-1.221	-0.102	-2.555	-12.035	-2.455	-6.395
Nb	-1.767	-0.062	-3.104	-12.630	-3.044	-6.899
Ni	-0.634	-0.513	-2.026	-11.489	-1.943	-5.838
Os	-2.301	-1.203	-2.887	-12.388	-2.806	-6.761
Pd	0.317	-1.132	-1.854	-11.378	-1.849	-5.750
Pt	-1.049	-1.188	-1.931	-11.358	-1.883	-5.799
Re	-1.443	-0.206	-2.305	-11.768	-2.285	-6.161
Rh	-0.343	-0.951	-2.233	-11.719	-2.184	-6.075
Ru	-1.083	-1.070	-2.701	-12.250	-2.637	-6.619
Sc	-0.701	0.966	-2.609	-12.041	-2.498	-6.455
Ta	-2.692	-0.598	-3.246	-12.806	-3.066	-7.132
Tc	-0.607	-0.251	-2.113	-11.624	-2.024	-5.965
Ti	-1.117	1.108	-2.101	-11.615	-1.988	-5.929
V	-1.714	0.124	-2.727	-12.210	-2.643	-6.582
W	-2.188	-0.379	-2.765	-12.365	-2.708	-6.637
Y	-0.949	1.260	-2.651	-12.215	-2.606	-6.516
Zr	-1.419	0.963	-2.192	-11.710	-2.071	-5.947

Table S2 Input features (band centers, eV) of SISSO of $TM_1@WSe_2$-Se catalysts.

	M-s	M-d	Se_{23}-p	Se_1-s	Se_{36}-p	W_{52}-s
Co	-1.962	-1.029	-2.704	-12.401	-2.525	-6.261
Cr	-1.069	0.720	-2.630	-12.317	-2.437	-6.165
Fe	-2.290	-1.165	-3.015	-12.719	-2.813	-6.640
Hf	-1.801	0.945	-2.380	-12.130	-2.202	-6.015
Ir	-2.518	-1.500	-2.517	-12.166	-2.241	-6.015
Mn	-0.949	-0.005	-2.213	-11.943	-2.064	-5.744
Mo	-1.514	-0.219	-2.678	-12.405	-2.557	-6.280
Nb	-1.966	-0.473	-3.335	-12.940	-3.257	-6.677
Ni	-1.305	-0.780	-2.134	-11.845	-1.987	-5.648
Os	-2.742	-1.317	-2.656	-12.402	-2.288	-6.304
Pd	-0.417	-1.552	-2.030	-11.742	-1.932	-5.554
Pt	-1.861	-1.735	-2.098	-11.793	-1.908	-5.655
Re	-2.437	-0.699	-2.578	-12.314	-2.450	-6.034
Rh	-1.166	-1.202	-2.370	-12.062	-2.126	-5.915
Ru	-1.686	-1.315	-2.774	-12.438	-2.520	-6.366
Sc	-0.787	1.237	-2.784	-12.418	-2.595	-6.192
Ta	-2.921	-0.781	-3.443	-13.183	-3.317	-7.026
Tc	-0.940	-0.201	-2.303	-12.027	-2.158	-5.949
Ti	-1.157	0.953	-2.342	-12.077	-2.171	-6.222
V	-2.033	0.078	-2.946	-12.706	-2.807	-6.497
W	-2.898	-0.704	-3.057	-12.801	-2.884	-6.782
Y	-1.109	1.050	-2.819	-12.528	-2.584	-6.312
Zr	-1.240	0.935	-2.388	-12.059	-2.212	-5.891

Table S3 Input features (band centers, eV) of SISSO of $TM_1@WS_2$-S catalysts.

	M-s	M-d	S_{23}-p	S_1-s	S_{36}-p	W_{52}-s
Co	-1.531	-0.902	-2.795	-12.204	-2.581	-7.040
Cr	-0.705	0.857	-2.887	-12.178	-2.707	-6.982
Fe	-2.037	-1.393	-3.521	-12.816	-3.378	-7.629
Hf	-1.408	1.063	-2.530	-11.924	-2.381	-6.715
Ir	-2.052	-1.443	-2.635	-11.911	-2.427	-6.763
Mn	-0.714	-0.004	-2.406	-11.731	-2.221	-6.553
Mo	-0.981	-0.086	-2.863	-12.185	-2.701	-7.000
Nb	-1.345	-0.047	-3.314	-12.745	-3.275	-7.396
Ni	-1.053	-0.299	-2.322	-11.607	-2.119	-6.358
Os	-2.650	-1.492	-3.186	-12.526	-3.004	-7.290
Pd	-0.027	-1.319	-2.136	-11.638	-2.016	-6.335
Pt	-1.536	-1.426	-2.292	-11.472	-2.118	-6.349
Re	-1.950	-0.427	-2.685	-11.975	-2.526	-6.688
Rh	-0.621	-1.207	-2.506	-11.848	-2.427	-6.623
Ru	-1.332	-1.358	-2.992	-12.273	-2.883	-7.107
Sc	-0.405	1.531	-3.049	-12.441	-2.855	-7.309
Ta	-2.859	-0.647	-3.767	-13.068	-3.602	-7.857
Tc	-0.693	-0.262	-2.457	-11.811	-2.295	-6.658
Ti	-0.831	1.038	-2.487	-11.829	-2.245	-6.671
V	-1.518	0.069	-3.117	-12.450	-2.946	-7.229
W	-2.390	-0.542	-3.139	-12.499	-3.023	-7.297
Y	-0.629	1.372	-3.094	-12.336	-2.812	-7.155
Zr	-2.175	0.179	-2.839	-12.232	-2.637	-6.993

Table S4 Input features (band centers, eV) of SISSO of TM_1@$MoSe_2$-Se catalysts.

	M-s	M-d	Se_{23}-p	Se_1-s	Se_{36}-p	Mo_{52}-s
Co	-1.789	-1.015	-2.442	-12.314	-2.215	-6.264
Cr	-1.092	0.367	-2.444	-12.338	-2.231	-6.227
Fe	-2.118	-1.671	-2.867	-12.885	-2.689	-6.790
Hf	-2.169	0.590	-2.190	-12.126	-1.967	-5.946
Ir	-1.896	-1.379	-2.176	-12.123	-2.005	-6.118
Mn	-1.171	-0.137	-2.028	-11.903	-1.800	-5.812
Mo	-1.953	-0.282	-2.546	-12.465	-2.353	-6.325
Nb	-2.650	-0.389	-3.110	-12.925	-2.924	-6.834
Ni	-1.075	-0.496	-1.893	-11.827	-1.770	-5.813
Os	-2.567	-1.697	-2.722	-12.634	-2.570	-6.549
Pd	-0.206	-1.257	-1.835	-11.719	-1.634	-5.648
Pt	-1.301	-1.350	-1.817	-11.687	-1.673	-5.651
Re	-2.072	-0.420	-2.280	-12.212	-2.182	-6.094
Rh	-1.091	-1.081	-2.107	-12.069	-1.920	-5.950
Ru	-1.939	-1.356	-2.590	-12.530	-2.402	-6.494
Sc	-1.524	1.448	-2.559	-12.315	-2.338	-6.105
Ta	-3.387	-0.863	-3.112	-13.043	-3.007	-6.893
Tc	-1.440	-0.264	-2.051	-11.994	-1.862	-5.930
Ti	-1.857	0.900	-2.076	-12.036	-1.946	-5.889
V	-2.343	0.002	-2.686	-12.628	-2.501	-6.512
W	-2.846	-0.675	-2.823	-12.757	-2.647	-6.616
Y	-1.619	1.016	-2.532	-12.466	-2.330	-6.341
Zr	-2.069	0.692	-2.155	-12.097	-1.944	-5.935

Table S5 Input features (band centers, eV) of SISSO of $TM_1@MoS_2$-Mo catalyst.

	M-s	M-d	S_{19}-p	Mo_{69}-s
Co	-7.088	-2.092	-2.446	-6.51
Cr	-7.088	-2.092	-2.446	-6.51
Fe	-7.032	-1.604	-2.598	-6.587
Hf	-5.563	-0.788	-1.902	-6.065
Ir	-7.604	-3.428	-2.905	-6.924
Mn	-7.092	-1.579	-2.805	-6.846
Nb	-4.808	0.679	-1.864	-5.811
Ni	-5.441	-1.997	-2.364	-6.402
Os	-7.812	-3.2	-3.156	-7.14
Pd	-5.423	-2.952	-2.518	-6.543
Pt	-7.223	-4.291	-2.757	-6.764
Re	-8.195	-2.638	-3.402	-7.382
Rh	-6.634	-3.044	-2.791	-6.821
Ru	-7.195	-2.666	-3.063	-7.09
Sc	-4.311	1.829	-1.966	-6.058
Ta	-5.554	-0.135	-1.881	-5.833
Ti	-5.57	1.019	-1.979	-6.007
V	-5.72	0.513	-1.911	-5.822
W	-6.197	-0.642	-1.86	-5.804
Y	-3.112	-0.271	-1.867	-6.095
Zr	-5.405	0.661	-1.846	-5.814

277 **Table S6** Input features of SISSO of $TM_1@WSe_2$-W catalysts.

	M-s	W_{56}-p	ΔG_{*H}
Co	-5.944	-4.149	-0.206
Cr	-5.205	-3.477	1.213
Fe	-5.651	-4.009	0.464
Hf	-4.773	-3.494	0.652
Ir	-6.498	-4.242	-0.165
Mn	-5.925	-4.253	0.649
Mo	-5.111	-3.535	2.037
Nb	-4.546	-3.615	0.695
Ni	-5.395	-3.817	0.422
Os	-6.686	-4.469	0.463
Pd	-4.799	-3.833	-0.161
Pt	-5.629	-3.877	-0.104
Re	-6.993	-5.047	0.750
Rh	-5.669	-4.28	-0.265
Ru	-6.019	-4.332	0.388
Sc	-3.303	-3.595	0.626
Ta	-4.939	-3.415	0.733
Ti	-5.033	-3.777	0.602
V	-4.993	-3.483	0.592
Y	-3.132	-3.221	0.615
Zr	-4.518	-3.497	0.606

278

Table S7 Band centers (eV) of metal sites in $TM_1@MoS_2$-S and $TM_1@WSe_2$-Se.

	S-vac: M				Se-vac: M			
	ε_s	ε_p	ε_d		ε_s	ε_p	ε_d	$\varepsilon_{M\text{-}d} - \varepsilon_{M\text{-}d}$
Co	-1.27	-0.03	-0.91	Co	-1.96	-0.14	-1.03	0.12
Cr	-0.46	-0.03	0.78	Cr	-1.07	0.03	0.72	0.06
Fe	-1.77	-0.63	-1.81	Fe	-2.29	-0.46	-1.17	-0.64
Hf	-1.54	-0.14	0.95	Hf	-1.80	-0.01	0.95	0.01
Ir	-1.65	0.23	-1.19	Ir	-2.52	0.18	-1.50	0.31
Mn	-0.48	0.66	0.16	Mn	-0.95	0.56	-0.01	0.16
Nb	-1.77	-1.10	-0.06	Nb	-1.97	-0.98	-0.47	0.41
Ni	-0.63	0.60	-0.51	Ni	-1.31	0.55	-0.78	0.27
Os	-2.30	-0.38	-1.20	Os	-2.74	-0.02	-1.32	0.11
Pd	0.32	0.86	-1.13	Pd	-0.42	0.82	-1.55	0.42
Pt	-1.05	0.78	-1.19	Pt	-1.86	0.67	-1.74	0.55
Re	-1.44	0.16	-0.21	Re	-2.44	0.07	-0.70	0.49
Rh	-0.34	0.39	-0.95	Rh	-1.17	0.44	-1.20	0.25
Ru	-1.08	-0.24	-1.07	Ru	-1.69	-0.04	-1.32	0.25
Sc	-0.70	-0.27	0.97	Sc	-0.79	-0.05	1.24	-0.27
Ta	-2.69	-1.22	-0.60	Ta	-2.92	-1.03	-0.78	0.18
Ti	-1.12	0.41	1.11	Ti	-1.16	0.56	0.95	0.16
V	-1.71	-0.62	0.12	V	-2.03	-0.37	0.08	0.05
Y	-0.95	-0.35	1.26	Y	-1.11	-0.20	1.05	0.21
Zr	-1.42	0.68	0.96	Zr	-1.24	0.76	0.94	0.03

Table S8 Band centers (eV) of S/Se sites in $TM_1@MoS_2$-Mo and $TM_1@WSe_2$-W.

	Mo-vac: S				W-vac: Se			
	ε_s	ε_p	ε_d		ε_s	ε_p	ε_d	$\varepsilon_{S\text{-}p} - \varepsilon_{Se\text{-}p}$
Co	-12.06	-2.44	-	Co	-11.87	-2.41	-	-0.03
Cr	-12.06	-2.44	-	Cr	-11.16	-1.57	-	-0.87
Fe	-12.22	-2.63	-	Fe	-11.74	-2.25	-	-0.38
Hf	-11.54	-1.91	-	Hf	-10.94	-1.68	-	-0.23
Ir	-12.49	-2.99	-	Ir	-12.02	-2.46	-	-0.53
Mn	-12.45	-2.88	-	Mn	-11.96	-2.43	-	-0.44
Nb	-11.22	-1.80	-	Nb	-11.06	-1.48	-	-0.32
Ni	-11.44	-2.05	-	Ni	-10.99	-1.73	-	-0.32
Os	-12.89	-3.38	-	Os	-12.06	-2.53	-	-0.84
Pd	-11.96	-2.19	-	Pd	-8.32	-1.58	-	-0.62
Pt	-12.42	-2.92	-	Pt	-7.97	-1.16	-	-1.76
Re	-13.22	-3.60	-	Re	-12.69	-3.11	-	-0.49
Rh	-12.29	-2.74	-	Rh	-11.80	-2.07	-	-0.67
Ru	-12.60	-3.00	-	Ru	-11.82	-2.25	-	-0.75
Sc	-11.45	-1.88	-	Sc	-10.88	-1.56	-	-0.33
Ta	-11.29	-1.86	-	Ta	-11.07	-1.62	-	-0.24
Ti	-11.27	-1.80	-	Ti	-11.08	-1.62	-	-0.18
V	-11.21	-1.73	-	V	-11.01	-1.52	-	-0.22
Y	-10.58	-1.51	-	Y	-11.14	-1.50	-	-0.01
Zr	-11.19	-1.76	-	Zr	-10.92	-1.64	-	-0.12

References

1 G. Kresse and J. Hafner, *Phys. Rev. B*, 1993, **47**, 558–561.

2 V. Wang, N. Xu, J. C. Liu, G. Tang and W.-T. Geng, *Comput. Phys. Commun.*, 2021, **267**, 108033.

3 G. Kresse and D. Joubert, *Phys. Rev. B*, 1999, **59**, 1758–1775.

4 J. P. Perdew, K. Burke and M. Ernzerhof, *Phys. Rev. Lett.*, 1996, **77**, 3865–3868.

5 J. P. Perdew, J. A. Chevary, S. H. Vosko, K. A. Jackson, M. R. Pederson, D. J. Singh and C. Fiolhais, *Phys. Rev. B*, 1992, **46**, 6671–6687.

6 S. Grimme, S. Ehrlich and L. Goerigk, *J. Comput. Chem.*, 2011, **32**, 1456–1465.

7 D. J. Chadi, *Phys. Rev. B*, 1977, **16**, 1746–1747.

8 J. K. Nørskov, J. Rossmeisl, A. Logadottir, L. Lindqvist, J. R. Kitchin, T. Bligaard and H. Jónsson, *J. Phys. Chem. B*, 2004, **108**, 17886–17892.

9 Y. Wang, A. J. Page, Y. Nishimoto, H.-J. Qian, K. Morokuma and S. Irle, *J. Am. Chem. Soc.*, 2011, **133**, 18837–18842.

10 G. Di Liberto, L. A. Cipriano and G. Pacchioni, *J. Am. Chem. Soc.*, 2021, **143**, 20431–20441.

11 J. Rossmeisl, A. Logadottir and J. K. Nørskov, *Chem. Phys.*, 2005, **319**, 178–184.

12 J. Greeley, T. F. Jaramillo, J. Bonde, I. Chorkendorff and J. K. Nørskov, *Nat. Mater.*, 2006, **5**, 909–913.

13 R. Parsons, *Trans. Faraday Soc.*, 1958, **54**, 1053.

14 J. K. Nørskov, T. Bligaard, A. Logadottir, J. R. Kitchin, J. G. Chen, S. Pandelov and U. Stimming, *J. Electrochem. Soc.*, 2005, **152**, J23.

15 R. Huang, M. F. Hanif, M. K. Siddiqui, M. F. Hanif and F. B. Petros, *Sci. Rep.*, 2024, **14**, 26552.